

Article

Experimental Verification of Methods for Converting Acceleration Data in High-Rise Buildings into Displacement Data by Shaking Table Test

Heuisoo Han ¹, Mincheol Park ^{1,*}, Sangki Park ² , Juhyong Kim ² and Yong Baek ²¹ Kumoh National Institute of Technology, Gumi-si 39177, Korea; hanhs@kumoh.ac.kr² Korea Institute of Civil Engineering and Building Technology, 283, Goyang-daero, Ilsanseo-gu, Goyang-si 10223, Gyeonggi-do, Korea; skpark@kict.re.kr (S.P.); haitink@kict.re.kr (J.K.); baek44@kict.re.kr (Y.B.)

* Correspondence: parkmincheol84@gmail.com; Tel.: +82-54-478-7618

Received: 23 January 2019; Accepted: 16 April 2019; Published: 21 April 2019



Abstract: When diagnosing damage to high-rise buildings during earthquakes, it is necessary to measure the displacement of each story. However, with respect to accuracy and cost, it is most reasonable to convert acceleration into displacement. In this study, shake table testing was carried out to verify the conversion methods, converting the acceleration data measured in a high-rise building into velocity and displacement. In the shaking table test, the displacement of a 10-story model building under strong motion was measured using high-speed imaging devices. High-speed images were taken at 1000 frames per second, reflecting the dynamic behavior of the model building. Then, this displacement was compared with the displacement obtained by processing the acceleration data. This study applied three methods for correcting and converting acceleration into velocity and displacement. Method 1 used the transfer function, $H_2(\omega)$, which reflects the dynamic characteristics of the system. The displacements converted by this method showed the lowest accuracy, because the transfer function depends on the dynamic characteristics of the structure. Method 2 used the cosine Fourier transform for baseline correction, and the discrete input data are calculated as the sum of the cosine functions. Method 3 used the least-squares fitting in the first step to remove the linear drift in the acceleration and applied the high-pass Butterworth filter. The displacements converted by Method 2 were the most reliable, and were close to the displacements measured in the shaking table test. However, the response of high-rise buildings is affected by low- and high-frequency noise. It is necessary to further investigate the limitations and applicability of the conversion methods for providing reliable displacement of the building.

Keywords: high-rise building; acceleration data; shaking table test; conversion method; baseline correction

1. Introduction

The raw ground motion signals recorded by seismologists are always preprocessed before any engineering and seismological analysis takes place. Strong-motion data processing has two main objectives in making the data useful for engineering analysis: (1) correction of the strong motion sensor itself (analogue or digital sensors can be used), and (2) reduction of random noise in the recorded signals [1]. Different authors and agencies around the world have used a variety of steps in data processing. The three major organizations in the United States for seismic analysis, the USGS (US Geological Survey), PEER (Pacific Earthquake Engineering Research Centre), and CSMIP (California Strong-Motion Instrumentation Program), also use different signal processing techniques to process records [2]. Other European countries have also reported the specific data processing steps that

they have adopted [3]. Mollova (2006) presented the application of digital filtering in the data processing of acceleration records from earthquakes, whereby Butterworth, Chebyshev, and Bessel filters with different orders were employed to eliminate noise. One dataset under investigation included accelerograms from three stations located in Turkey, Dinar, Izmit, and Kusadasi, withal of which use an analogue seismograph, SMA-1 [2]. Jones et al., (2018) presented the Processing and Review Interface for Strong Motion data (PRISM) software, developed by the National Strong Motion Project (NSMP) of the U.S. Geological Survey (USGS) [4]. Corrected acceleration, velocity, and displacement time series could be obtained by applying baseline correction methods and filtering to ensure that the spectral content of the resulting products was within the sensors' frequency response range, and exhibited a signal-to-noise ratio (SNR) significantly improved with respect to the expected background noise level [5,6]. In the United States and Europe, much research has been done on strong-motion data processing with the aim of accurately evaluating ground motion [7–10]. Seismometers are able to measure the vertical and horizontal components of earthquakes. Analogue filters can be used for the data processing of analogue seismometers, with Butterworth [11] and Chebyshev filters being the most typical analogue filters used. The resulting frequency characteristics are thus referred to as Butterworth and Chebyshev characteristics, respectively [12].

This signal processing can be carried out for the seismological analysis of ground motion by seismologists. However, to perform a diagnosis of the structure, an accelerometer is installed in high-rise buildings [13]. In order to carry out the diagnosis and health monitoring of high-rise buildings, the raw data measured by the accelerometer must be analyzed by seismologists directly, without preprocessing. This is because noise is generated due to the dynamic characteristics of the structure, as well as artificial factors such as walking and machine operation. Noise needs to be removed from the measured acceleration data, and the displacement should be calculated with baseline correction. Then, the converted displacement can be used to evaluate the baseline drift of the high-rise building. Therefore, acceleration must be converted into velocity and displacement through filtering and baseline correction.

The causes and characteristics of noise and baseline drift are as follows. Low-frequency signals, including acceleration, velocity, and displacement waveforms, are as crucial as high-frequency signals for many areas of study in the fields of seismology and earthquake engineering. For example, velocity signals are associated with the kinetic energy of seismic waves, and low-frequency seismic waves contribute substantially to the responses of high-rise buildings, as well as huge structures such as dams and bridges. Unfortunately, these low-frequency seismic waves are easily contaminated by baseline errors. Most baseline errors in seismic signals are negligible with respect to acceleration, but become larger with respect to velocity and displacement waveforms. A displacement waveform based directly on the integration of the raw accelerograms, without applying any preprocessing, may deviate greatly from the baseline. Most of these baseline errors are much larger than the ground displacement itself, and as such, they are larger than the limits for the usefulness of low-frequency signals. Therefore, baseline correction is an essential step in extracting more low-frequency information from strong-motion accelerograms [14].

Figure 1 shows the results of the numerical calculation of velocity and displacement from acceleration without baseline correction or filtering, measured by means of the shaking table test. The figure shows that the converted displacement is unreliable. In this paper, the abbreviation AVD (Acceleration-Velocity-Displacement) is used to refer to the conversion of acceleration into velocity and displacement. Velocity can be obtained by integrating acceleration, while displacement can be obtained either through the integration of velocity or a double integration of acceleration. However, this basic principle of physics is not valid for disseminated data acquired from various strong-motion data providers [15]. Chiu (2012) examined several examples, which included three sets of three-component waveforms disseminated by the Berkeley Digital Seismic Network (BDSN), the National Strong-Motion Program of the US Geological Survey (USGS), and the California Strong-Motion Instrumentation Program of the California Geological Survey (CGS). The displacement waveforms were different from

the corresponding velocity waveforms, which showed a significant linear baseline drift. Therefore, the initial data for velocity and displacement were assumed to be zero in order to remove the linear baseline drift [15]. This incompatibility appears not only in displacement data, but also in data derived from acceleration, such as in long-period response spectra [16]. Pecknold and Riddell [17,18] also found that incompatible acceleration may lead to low-frequency distortion in the calculation of structural response, and this effect becomes more serious in nonlinear cases [18]. The idea underlying signal processing is the removal of noise from strong-motion data in order to be able to extract valuable information, such as peak ground characteristics and response spectra. Although noise causes distortion of the true signal over a wide frequency range, its influence is more dramatic in the low- and high-frequency ranges, where the signal-to-noise ratio tends to be significantly lower. Nowadays, in the signal processing of strong motion, frequencies lower than 1 Hz and higher than 20 Hz are regarded as low- and high-frequency limits, respectively [19]. Athanasiou et al. (2018) removed low-frequency noise using a simple baseline-fitting scheme. The signal-processing scheme they developed and used defines the duration of the main event, removes background noise, and adjusts the distorted baseline drift using a polynomial curve.

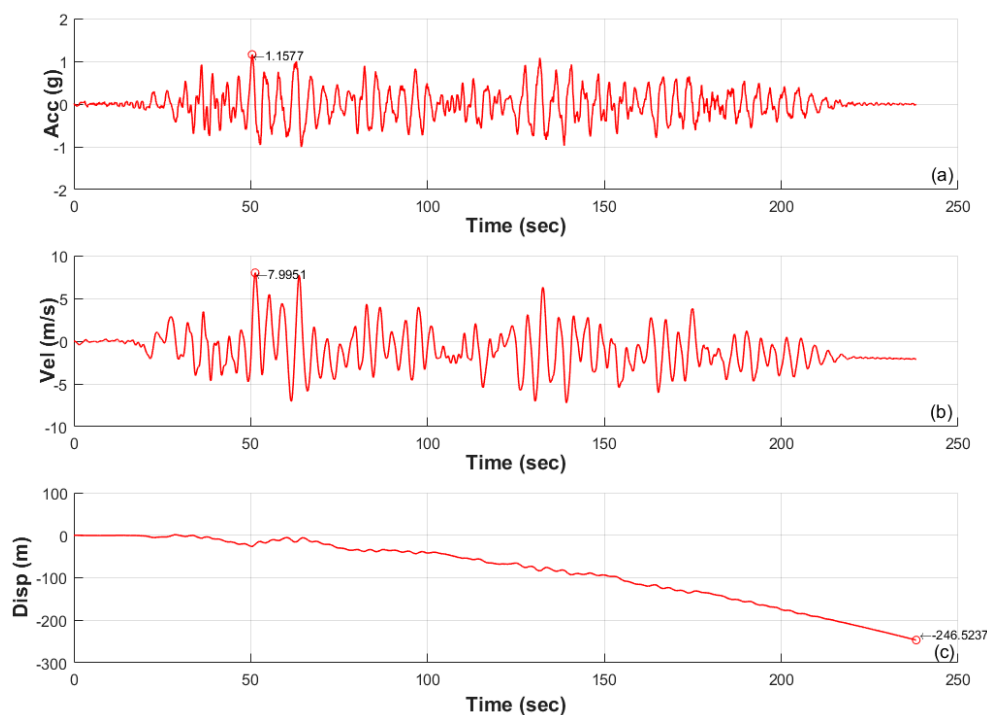


Figure 1. Results of the numerical integration of velocity and displacement without baseline correction from the acceleration measured in the shaking table test; (a) Acceleration; (b) Velocity; (c) Displacement.

Several previous studies have reported the error and baseline drift in earthquake accelerometer records; these can be caused by various factors arising from the vicinity of the location at which the earthquake accelerometer is installed [14–19]. The frequency band is distributed over a wide range, from 0.001 to several tens of Hz. Generally, low-frequency noise below about 0.1 Hz is called a microseism, and high-frequency noise from 0.5 to several tens of Hz is referred to a microtremor [20]. Generally, noise in the range of 0.1 to 0.5 Hz is caused by waves on the sea surface, and becomes weaker as the distance from the coast gets greater. Noise lower than 0.1 Hz is known to be the main cause of changes in micro-pressure [21,22]. By contrast, high-frequency noise above 1 Hz is typically caused by transportation and industrial facilities, other human factors, and natural factors, such as wind and waves [23,24]. In particular, high-rise buildings are greatly influenced by natural factors such as wind, as well as artificial factors due to mechanical vibration and walking load.

Previous research on strong motion has identified the causes of noise in the frequency domain of accelerometers [14]. A variety of processing and filtering techniques have been developed to compensate for seismic accelerometers [15,25]. However, not much research has been done on correction and filtering methods for accelerometers installed in high-rise buildings. The data obtained from accelerometers installed in a free field depend on the characteristics of the ground, and the artificial influence is relatively small. However, artificial factors have a great influence on the noise and dynamic characteristics of high-rise buildings. Therefore, it is necessary to verify the method by which acceleration data of high-rise buildings is converted into displacement data. In particular, acceleration measured over long periods leads to large error and baseline drift in displacement in the diagnostic assessment of high-rise buildings. The displacement of high-rise buildings can be measured by GPS, but high accuracy is required for soundness assessment, and the corresponding GPS is very expensive. High-speed imaging can measure the displacement of a structure, but it is difficult to perform measurements at all times, and challenging to apply this technique to high-rise buildings [26]. Therefore, it is most efficient to install an accelerometer in high-rise buildings and convert this data into displacement.

In this study, the shaking table test was performed to verify the conversion methods. This involves converting the data from an accelerogram installed in a tall building into velocity and displacement data. In the shaking table test, the displacement of a 10-story model building under strong motion was measured using high-speed imaging. High-speed images were taken at 1000 frames per second, capturing the dynamic behavior of the model building. Then, this displacement was compared with the displacement obtained by processing the acceleration data. This study applied three methods for correcting and converting acceleration to velocity and displacement. The characteristics and the applicability of the conversion methods for carrying out diagnosis of high-rise buildings are evaluated in this study.

2. Experimental Setup and Processing Methods

2.1. Shaking Table Test

In general, the shaking table test is performed in order (1) to identify the dynamic characteristics of the target structure system, and (2) to obtain a validated analytical model. It can also be used (3) to verify the durability of the structure, and (4) to diagnose and maintain the integrity of the structure. Changes in the vibration characteristics of a structure often indicate a problem related to the structural integrity of the structure. For example, when a structure is subjected to a load and reaches fracture, a crack occurs. In this case, the natural frequency is significantly different from the case in which there is no crack. Therefore, if there is a significant change in the natural frequency, it can be predicted that the safety of the structure is likely to be a problem [27–31].

In this study, the shaking table test was performed in order to verify the method used to convert acceleration data into velocity and displacement.

Figure 2 shows the shaking table test of a high-rise building. The shaking table test consists of a shaking table, a scale model consisting of 10 stories above ground and three stories below, as well as four accelerometers and a high-speed camera. The displacements of the high-rise building were estimated by analyzing images taken by a high-speed camera. The acceleration data measured by the accelerometer were then converted into displacement and compared with the displacement by image analysis. Figure 2c shows a model of a shaking table and a high-rise building. The height of the model is 147.2 cm, the height above the ground surface (upper part) is 113.0 cm, and the depth below the ground surface (lower part) is 34.2 cm. The lower part is a square of 40 cm × 40 cm, and the upper part is a square of 20 cm × 20 cm. The accelerometer was installed at the base, 4th floor, 7th floor, and roof. The shaking table test was conducted by KICT (Korea Institute of Civil Engineering and Building Technology) in May 2018 at Smart C & S (Control & Sensing) in Daejeon, Korea. The model of the high-rise building was made without scale because there was no actual reference structure.

The input seismic waves were scaled considering the natural frequencies of the model, 1st = 2.8230 Hz, 2nd = 8.7980 Hz, and 3rd = 14.6990 Hz.

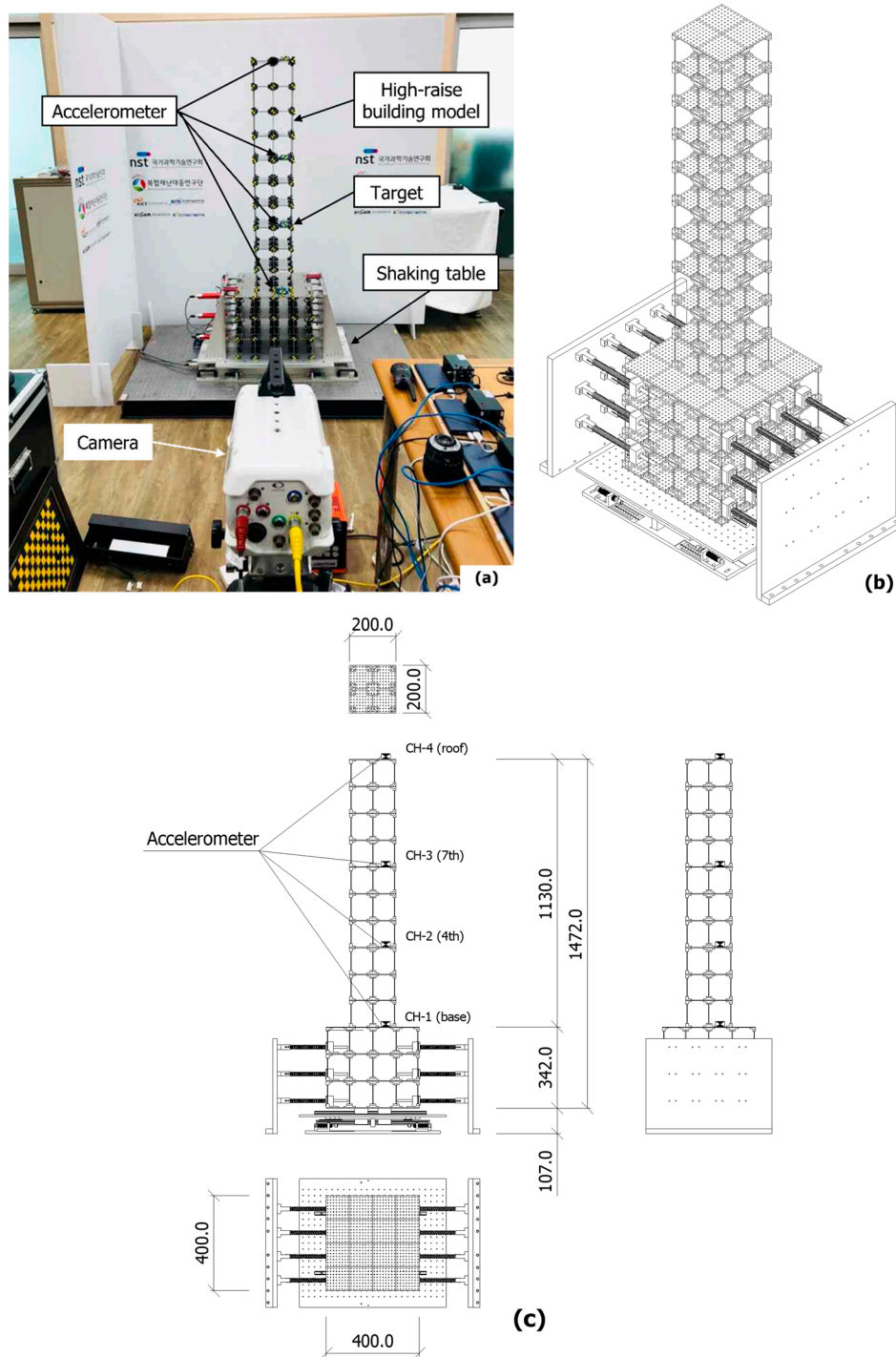


Figure 2. Shaking table test for verification of displacement conversion method of acceleration data; (a) Photo of experimental equipment; (b) 3D drawing; (c) 2D drawing.

The accelerometer used in the shaking table test was iLOG-MEMS-ACC, which is developed and sold by Smart C & S as shown in Figure 3. iLOG-MEMS-ACC is a wireless acceleration sensor system that rapidly sends (115.2 kbps) acceleration signals without noise, using Bluetooth. The sensor device consists of a 2-axis MEMS acceleration sensor, a 16 bit A/D converter, an 8 bit micro-controller, internal memory (2.0 MB), a Bluetooth communication module, and a Li-ion recharge module, which allows

self-acquisition of the acceleration signal, as well as decision-making according to an embedded algorithm. The detailed specifications of iLOG-MEMS-ACC are shown in Table 1.

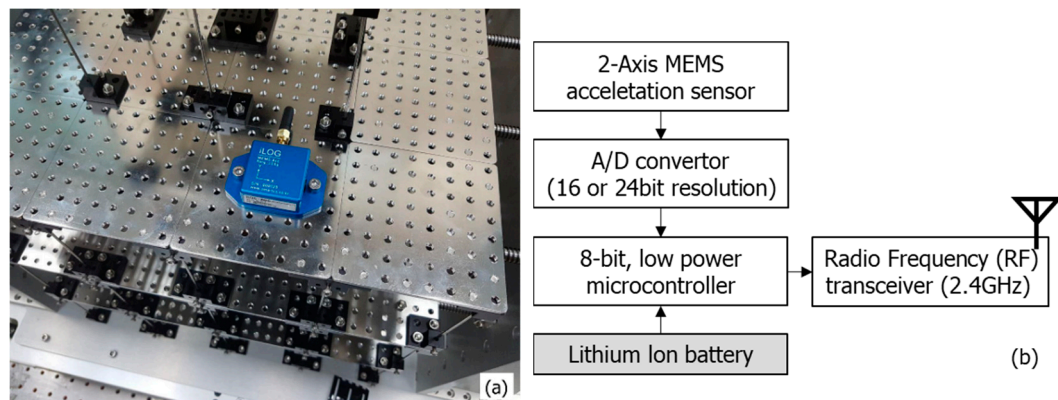


Figure 3. Pictures of (a) high-speed camera; (b) target.

Table 1. Detailed specification of acceleration (iLOG-MEMS-ACC) used in shaking table test.

Parameter	Specifications
Sensor input channels	Internal 2 or 3 axial MEMS ACC sensor
Resolution	16 bit resolution
Dynamic range	62.6 dB (typical)
MEMS Accelerometer Requirements	
Range	±1.2 g, ±2.0 g, ±3.0 g, ±5.0 g
Sensitivity	1000 mV/g, 420 mV/g, 300 mV/g, 174 mV/g
Noise Density	110 µg/rtHz, 250 µg/rtHz, 300 µg/rtHz, 250 µg/rtHz
Sampling	
Measurable signal bandwidth	0 Hz to 50 Hz (custom options available to 400 Hz)
Sampling rate	50 to 1200 SPS, 2400 SPS (Via iLOG-RECEIVER)
Operating Parameters	
Wireless communication range	Outdoor: 200 m (typical) Indoor: 50 m (typical)
Radio frequency (RF) transceiver carrier	2.4 Ghz to 2.4835 Ghz Bluetooth V2.0 + EDR Class 1
RF communication protocol	IEEE 802.15.1
RF Power	Max 18 dBm
Power source	Internal: 3.7 V 280 mA Li-po battery
Power consumption	0.5 W (Active mode)
Duration	2 h (Active mode)
Operating temperature	-20 °C to +60 °C
Physical Specifications	
Dimensions	64 mm × 41.5 mm × 18 mm
Weight	65 g
Enclosure material	Aluminum
Environmental rating	Indoor use

2.2. High-Speed Camera Shooting and Image Analysis

Table 2 and Figure 4 show the equipment used for high-speed camera shooting and image analysis, including a high-speed camera, targets, and an image analysis program. To estimate the displacements of super high-rise and complex facilities at the time of excitation, the high-speed camera was used for the image capture at 1000 frames per second and image analysis; (x, y, z) is the coordinate value of the tracker attached to the structure using a TEMA (Telecommunication Engineering and Manufacturing Association) image analysis program. The tracked tracker comprises the reference coordinate system, and then relative displacement is measured.

Table 2. Equipment and features used in high-speed camera shooting and image analysis.

Equipment Name	Model Name (Manufacturer)	Special Feature	Amount
High-speed camera	Phantom V641 (Vision research)	As a device capable of shooting over 1000 frames per second, it captures moments that cannot be observed by the human eye and analyzes the behavior of the structure using these records.	Two sets
Target		Easy-to-perceive Quadrant target & linear target in TEMA software	5 inch 3 inch 1 inch Linear
Image analysis program	TEMA (Image systems)	A program which can analyze length, speed, acceleration, angle, angular velocity, etc., through a captured image or images	1 EA



Figure 4. Pictures of (a) high-speed camera; (b) targets.

The test procedure for the image analysis and the high-speed camera setting procedure is described here. First, quadrant targets were attached to the corners of each layer in order to measure the three-axis displacement of each layer using a vibrating tester. The size of the target was chosen to be sufficiently large to identify and analyze each frame for a high-speed camera shooting. To measure three-dimensional coordinates using a high-speed camera image, two high-speed cameras should be used to start shooting at the same point in time. The target to be observed (target attached to each layer) should be captured on each camera image. The position of the camera should be adjusted so that the target does not deviate out of the image while the excited structure is moving. The camera angle is adjusted to be between 45 degrees and 180 degrees.

To correct the distortion caused by the lens curvature, which is a problem for all camera lenses, it is necessary to take certain calibration values (parameter values for distortion correction) by shooting the calibration board several times. A high-speed camera with a shooting speed of over 1000 frames per second has a limited shooting time, depending on resolution and frames per second, which depend on the camera’s performance. Since the high-speed camera used in this test requires 50 s of shooting per experiment, the resolution was set at 2560 × 1600 pixels.

The basic concept of image analysis is to obtain a tracking shot of the trackers (targets) in each image taken by the high-speed camera, separating each frame using the algorithm included in the image analysis program, and converting the frames into data for easy analysis before finally reporting it. The data obtained by the image analysis program include the distance, speed, acceleration, relative displacement, angle, and angular velocity of the tracker.

2.3. AVD Conversion Method

Method 1 is called the Penzien filter, and it uses DFT and $H_2(\omega)$ [32]. Method 2 uses the baseline correction and cosine correction filter [33]. Method 3 uses a least-square fitting and 4th-order Butterworth filter [14]. The Penzien filter in Method 1 is a filtering process using the Fourier transform

and transfer function, and it removes low-frequency noise by means of a high-pass filter. Method 2 computes the discrete data of the input seismic waves as the sum of the cosine functions by means of a cosine Fourier transform. In Method 3, the least-squares fitting implemented in the first step removes the linear drift in the acceleration. In this study, the long-term measurement of the acceleration of the high-rise building incorporates the error and drift of the baseline. This is the cause of some of the error in the measuring equipment, as well as the background noise.

At this point, it is instructive to once again solve for the steady-state harmonic response using the exponential form of a solution. Consider the general case of harmonic loading expressed in exponential form:

$$\ddot{v}(t) + 2\xi\omega\dot{v}(t) + \omega^2v(t) = \frac{p_0}{m} \exp[i(\omega t + \phi)] \tag{1}$$

where ϕ is an arbitrary phase angle in the harmonic loading function, ω is loading frequency, and ω is natural frequency. In dealing with completely general harmonic loads, especially for the case of periodic loading where the earthquake is expressed as a series of harmonic terms, it is essential to define the input phase angle for each harmonic; however, this is usually most conveniently accomplished by expressing the input in complex number form rather than on the basis of amplitude and phase angle. In this section, only a single harmonic loading term will be considered; therefore, its phase angle is arbitrarily taken to be zero for the sake of simplicity. Therefore, it need not be included in the loading expression [32].

The specific solutions of Equation (1) and its first and second-time derivatives are

$$v(t) = G \exp(i\omega t) \tag{2}$$

$$\dot{v}(t) = i\omega G \exp(i\omega t) \tag{3}$$

$$\ddot{v}(t) = -\omega^2 G \exp(i\omega t) \tag{4}$$

where G is a complex constant. To evaluate these, substitute Equations (2)–(4) into Equation (1), cancel out the common quantity, $\exp(i\omega t)$, in each term, substitute $\frac{k}{\omega^2}$ for m , and β for $\frac{\omega}{\omega}$, and solve for G , which yields

$$G = \frac{p_0}{k} \left[\frac{1}{(1 - \beta^2) + i(2\xi\beta)} \right] \tag{5}$$

$$G = \frac{p_0}{k} \left[\frac{1}{(1 - \beta^2) + i(2\xi\beta)} \right] = \frac{p_0}{k} \left[\frac{1}{\left(1 - \left(\frac{\omega}{\omega}\right)^2\right) + i2\xi\frac{\omega}{\omega}} \right] = \frac{p_0}{k} \left[\frac{1}{\left(\frac{\omega^2 - \omega^2}{\omega^2}\right) + i2\xi\frac{\omega}{\omega}} \right] = \frac{p_0}{k} \left[\frac{\omega^2}{\omega^2 - \omega^2 + i2\xi\omega\omega} \right] \tag{6}$$

Equation (5) is rearranged as Equation (7).

$$\therefore G = \frac{p_0}{k} \left[\frac{\omega^2}{\omega^2 - \omega^2 + i2\xi\omega\omega} \right] \tag{7}$$

Rearranging Equation (4), we similarly obtain Equation (8).

$$a(t) = -\omega^2 G \exp(i\omega t) = (-\omega^2 G) \cdot \exp(i\omega t) \tag{8}$$

where $-\omega^2 G$ is constant and $\int e^{-i\omega t} dt = \frac{1}{i\omega} \cdot e^{-i\omega t}$. Equations (2) and (3) can be expressed by Equations (9) and (10), respectively.

$$v(t) = \frac{1}{i\omega} (-\omega^2 G) \cdot \exp(i\omega t) \tag{9}$$

$$d(t) = \frac{1}{(i\omega)^2} (-\omega^2 G) \cdot \exp(i\omega t) = G \cdot \exp(i\omega t) \tag{10}$$

The complex constant of Equation (7) can be rewritten as Equation (11).

$$G = \frac{p_0}{k} \left[\frac{\omega^2}{\omega^2 - \bar{\omega}^2 + i2\xi\bar{\omega}\omega} \right] = \frac{p_0}{k} \cdot H_2(\omega) \tag{11}$$

By substituting Equation (11) into Equation (10), the displacement in the time domain can be calculated using Equation (12).

$$d(t) = \frac{p_0}{k} \cdot H_2(\omega) \cdot \exp(i\bar{\omega}t) \tag{12}$$

Here, $H_2(\omega)$ is a correction filter in the frequency domain.

$$H_2(\omega) = \left[\frac{\omega^2}{\omega^2 - \bar{\omega}^2 + i2\xi\bar{\omega}\omega} \right] \tag{13}$$

Since it is difficult to set the reference point (fixed point) in order to measure the temporal change, it is necessary to measure the temporal change of the acceleration, and then to calculate the displacement by integrating it twice. However, when the acceleration, including the measurement error, is integrated twice and integrated into the displacement, the displacement includes the amplified additional error, due to the two integral transformations.

In this study, numerical integration, such as Fourier transform, has been used to convert acceleration into velocity and displacement. The Fourier transform is more simply a numerical integration; it is the decomposition of a periodic loading into a harmonic series. Here, $H_2(\omega)$ is a correction filter in the frequency domain [32].

Figure 5 shows the flowchart for the conversion of the acceleration data in Method 1. The acceleration data measured in the time domain should be transformed by the Fourier transform function in order to convert them into the frequency domain.

$$A_f(\omega) = F\{a(t)\} \tag{14}$$

In addition, $A_f(\omega)$ is calculated again in order to correct the data in the frequency domain; $H_2(\omega)$ is the correction filter multiplied to obtain the corrected Fourier transformed function $A_c(\omega)$.

$$A_c(\omega) = H_2(\omega)A_f(\omega) \tag{15}$$

Then, velocity and displacement are calculated in the frequency domain.

$$V(\omega) = i\omega A_c(\omega) \tag{16}$$

$$D(\omega) = (i\omega)^2 A_c(\omega) \tag{17}$$

Finally, to convert them into velocity and displacement in the time domain, the inverse Fourier transform function is used.

$$v(t) = F^{-1}\{V(\omega)\} \tag{18}$$

$$d(t) = F^{-1}\{D(\omega)\} \tag{19}$$

In this process, the content of the original signal is modulated on the basis of the transform function, reflecting the system characteristics. After being passed through the high-pass filter used at this juncture, the low-frequency components are removed.

This solution, using the time domain method, solves the equation of motion in the time domain directly. In contrast, solutions that use the frequency domain method are obtained by converting the equation of motion in the time domain into the frequency domain. Generally, by using a Fourier transform to convert the equation of motion into the frequency domain, a solution can be found more efficiently than by finding it in the time domain. Moreover, by applying a discrete Fourier transform

(DFT) using a fast Fourier transform (FFT) algorithm with a Fourier transform, the integrals used in the Fourier transform can be easily and quickly processed.

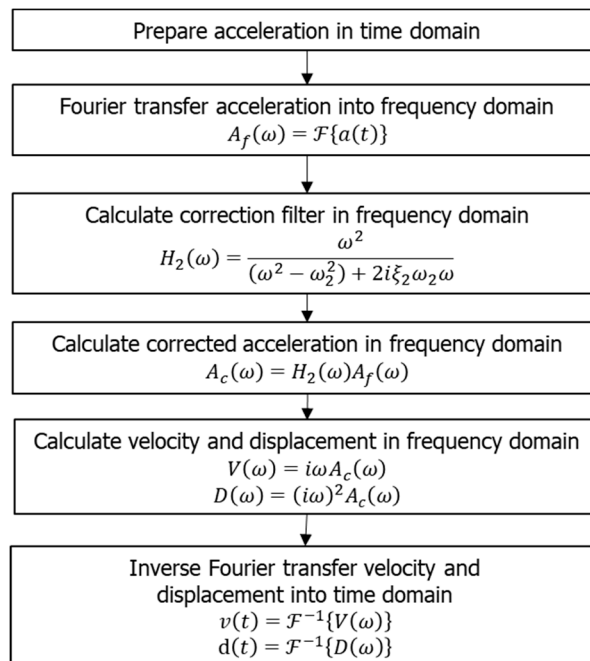


Figure 5. Flowchart for the conversion of acceleration data using Method 1.

The second method is time domain analysis. Figure 6 shows the flowchart for the conversion of acceleration data using Method 2. The load magnitude after the first load and the end of the measured load are assumed to be zero. There is zero padding. First, the acceleration (a_0) in the time domain is prepared and integrated so as to obtain the velocity (v_0) and the displacement (d_0). Next, a baseline correction of the initial acceleration (a_0) in the first-order linear equation is performed. c_0 and c_1 in Figure 6 are the coefficients of the first-order linear equation for the baseline correction. Then, the corrected acceleration ($a(t)$) is integrated in order to calculate the new velocity, ($v(t)$), and the displacement, ($d(t)$). Finally, the displacement ($d(t)$) is cosine-corrected. Using the cosine Fourier series transform, the discrete input data is calculated as the sum of the cosine functions.

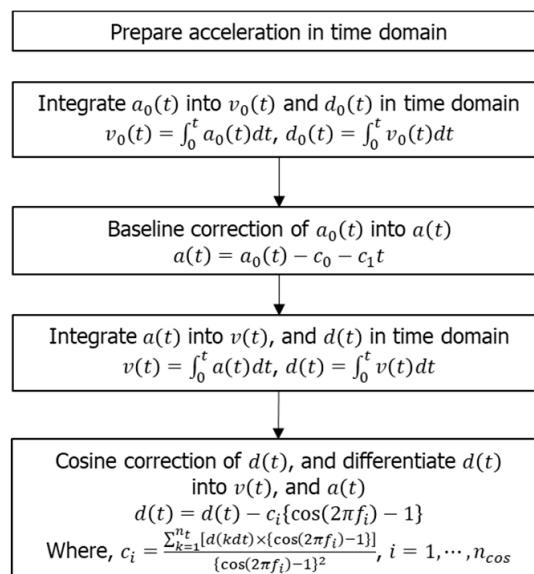


Figure 6. Flowchart for the conversion of acceleration data using Method 2.

The third method uses the least-square fitting and Butterworth filters for digital strong-motion data, as proposed by Chiu [14]. Figure 7 shows the flowchart for the conversion of acceleration data using Method 3, whereby $a_0(t)$ is the initial acceleration, $a(t)$ is the corrected acceleration, ω is natural frequency, ω_c is cutoff frequency, and G_0 is a frequency response at zero frequency. The least-squares fitting in the first step removes the linear trend of the acceleration. The long-term measurement of the acceleration of a high-rise building incorporates the errors and drift of the baseline. These are caused by errors in the measuring equipment, along with background error. The correction method for their removal consists of the following three steps. First, the baseline drift of the acceleration is removed using the least-squares method, and the acceleration in the time domain is converted into the frequency domain by Fourier transform. Next, low-frequency error is removed using the fourth-order Butterworth filter. The Butterworth filter does not generate a ripple in the passband; it has better performance than the Bessel filter, and the bandpass filter can simultaneously remove low-frequency and high-frequency noise. Because of these advantages, passband Butterworth filters are used in the PEER (Pacific Earthquake Engineering Research Centre) strong-motion database [34]. The Butterworth filter is also used in the Strong Motion data (PRISM) software developed by the US Geological Survey (USGS) [4]. The accelerometer installed in the high-rise building is an analogue system, and a typical analogue Butterworth filter is used. The last step required is to remove the linear trend that arises from having a nonzero initial velocity. When the strong-motion instrument records seismic data, those data may come from the effect of the background noise. To ensure that the strong motion records start from zero, the records should be processed by means of baseline initialization [35]. Furthermore, motions with very long periods must be sacrificed, and a combination of baseline correction and low-cut filtering can be used to produce motions that are accurate representations of the true ground motions obtained by many earthquake modelers [36].

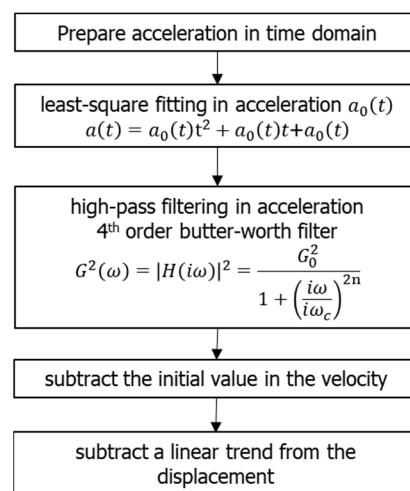


Figure 7. Flowchart for conversion of acceleration data in Method 3.

3. Shaking Table Test

3.1. Test Conditions

Figure 8 shows the excitation force of the shaking table test. In the test, the accelerations from three different earthquake—the Manjil earthquake, the Superstition Hills earthquake, and the Kobe earthquake—were used. These three sets of acceleration data were selected from the 22 earthquakes presented in FEMA P-695, taking place between 1974 and 1999 [37]. The Manjil earthquake occurred in 1990 in the city of Manjil in northern Iran. The shock had a moment magnitude of 7.4. The earthquake in Superstition Hills in California occurred in 1987, and had a magnitude of 6.6. The Kobe earthquake occurred in 1995. It measured 6.9 on the moment magnitude scale. These three earthquakes had in common that they occurred in the lower part of the metropolitan area. Because skyscrapers are

located in big cities, the acceleration data were selected from earthquakes that caused a great damage to large cities.

The accelerations and displacements of the structures generated during the excitation were measured by both accelerometer and high-speed imaging. The peak of the Manjil earthquake in Figure 8a is 0.4272 g, and the duration is 53.50 s. The peak of the Superstition Hills earthquake in Figure 8b is 0.45755 g, and the duration is 22.29 s. The peak of the Kobe earthquake in Figure 8c is 0.48557 g, and the duration is 40.95 s.

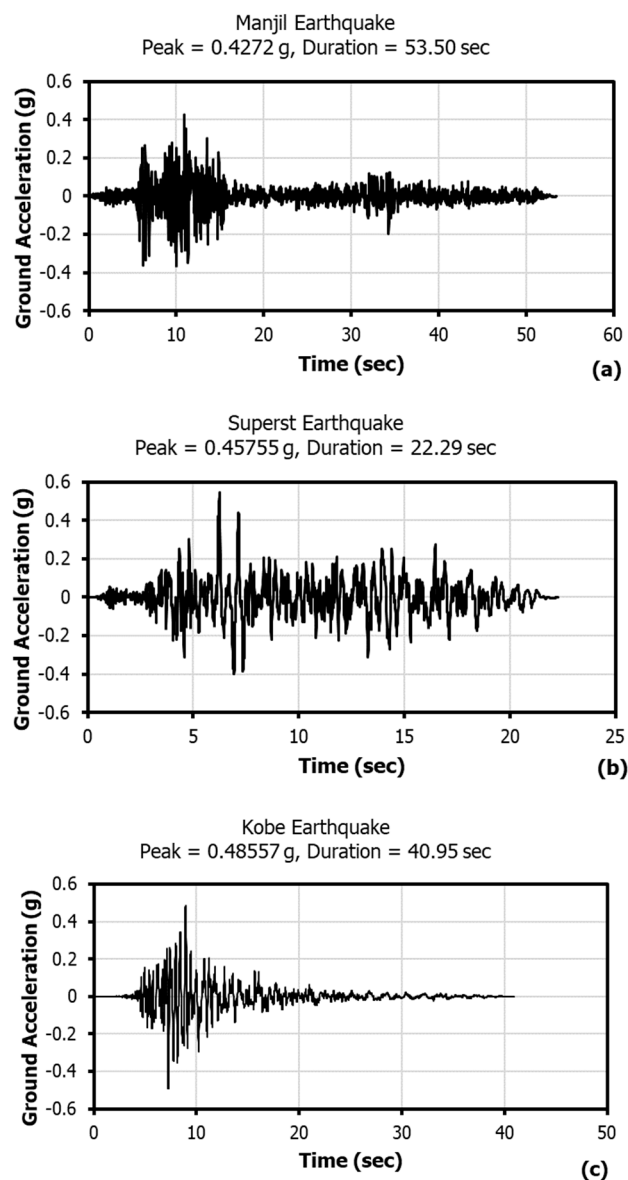


Figure 8. Earthquake input data for the Shaking Table Test; (a) Manjil earthquake; (b) Superstition Hills earthquake; (c) Kobe earthquake.

3.2. Experimental Response with Application of Strong Motion

Figure 9 shows the structural response and roof displacement for the Manjil earthquake, as measured during the shaking table test. The highest acceleration occurred at the top layer, and the displacement of the top layer, determined by high-speed imaging and analysis, was up to 141.4 mm. The resulting acceleration of the measured structure was entered into the code, converted to displacement, and compared with the measured roof displacement.

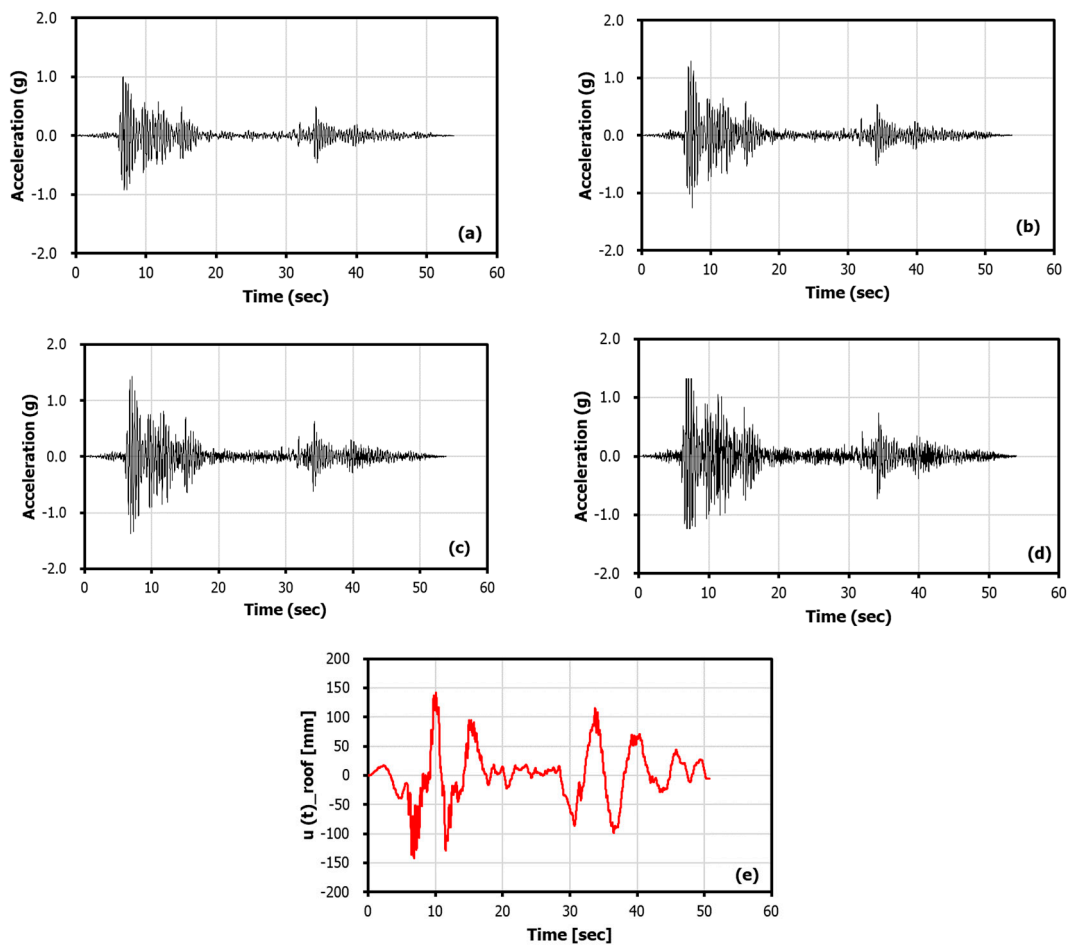


Figure 9. Dynamic response and roof displacement of the model for the Manjil earthquake; (a) base acceleration, (b) 4th floor acceleration, (c) 7th floor acceleration, (d) roof acceleration, and (e) roof displacement.

Figure 10 shows the response of the Superstition Hills earthquake and the roof displacement measured during the shaking table test. The highest acceleration was generated at the top layer, like in the Manjil earthquake, and the maximum displacement was 142.4 mm, as measured through high-speed imaging and analysis. The peak excitation of the Manjil earthquake was 0.4272 g, and the peak excitation of the Superstition Hills earthquake was 0.45755 g. The maximum displacement of the Superstition Hills earthquake was almost equal to the displacement caused by the Superstition Hills earthquake.

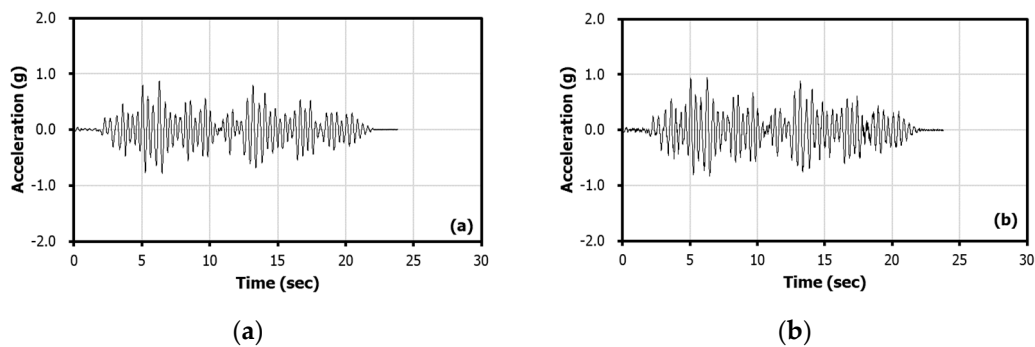


Figure 10. Cont.

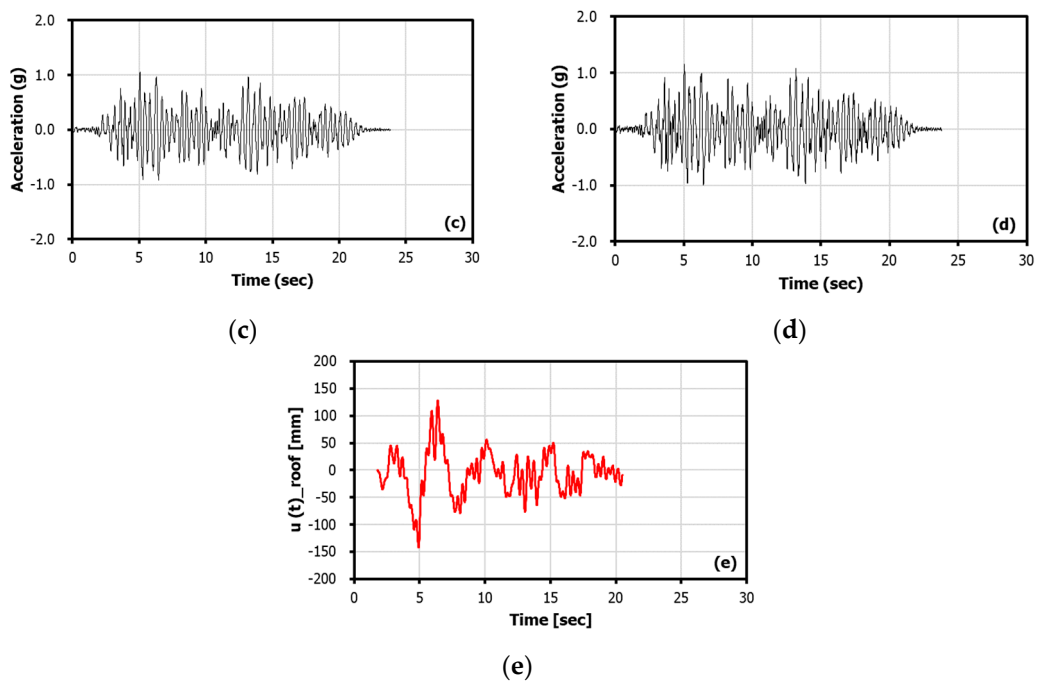


Figure 10. Dynamic response and roof displacement of the model for the Superstition Hills earthquake; (a) base acceleration, (b) 4th floor acceleration, (c) 7th floor acceleration, (d) roof acceleration, and (e) roof displacement.

Figure 11 shows the structural response and top layer displacement for the Kobe earthquake, as measured during the shaking table test. The highest acceleration occurred at the roof, like in the previously examined Manjil and Superstition Hills earthquakes, and the displacement of the uppermost layer as determined by high-speed imaging and analysis was up to 99.4 mm.

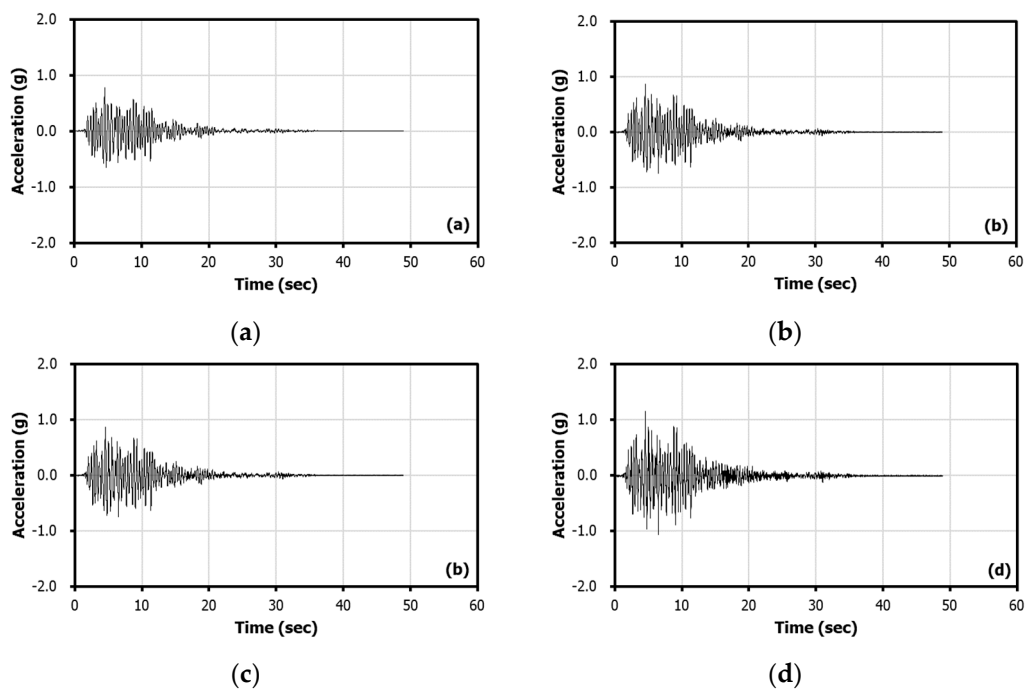


Figure 11. Cont.

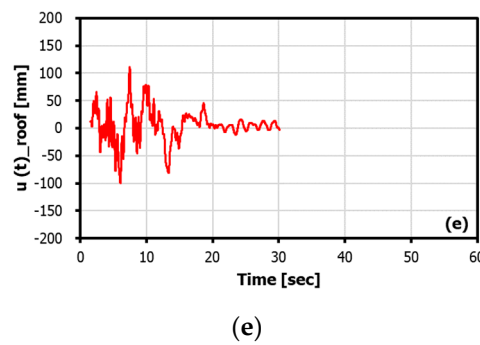


Figure 11. Dynamic response and roof displacement of the model for the Kobe earthquake; (a) base acceleration, (b) 4th floor acceleration, (c) 7th floor acceleration, (d) roof acceleration, and (e) roof displacement.

3.3. Conversion Process of Each Method

Three different conversion methods were used for this research, as already described in “2.3. AVD Conversion Method”. The techniques used in each method are shown in Table 3.

Table 3. Techniques for AVD conversion methods.

Method	Filter	Technique
1	Penzien filter	DFT $H_2(\omega)$ Frequency-domain
2	Cosine correction filter	Zero padding Baseline correction (1st order) Cosine correction filter Time-domain
3	Butter-worth filter	Least-square fitting Butter-worth filter (4th order) Frequency-domain

3.3.1. Method 1

The acceleration response measured three times on the basis of the applied force is converted into velocity and displacement using the Penzien filter in Figures 12–14. A description of the conversion steps and the graphs of the results are provided below.

First, the applied load is discretized. The duration of the acceleration (t_d) input for the shaking table test was 53.50 s for the Manjil earthquake, 22.29 s for the Superstition Hills earthquake, and 40.95 s for the Kobe earthquake. The measured time interval (Δt) was 0.05 s. The Manjil earthquake had 10784, the Superstition Hills earthquake had 4764, and the Kobe earthquake had 9784 data points. Therefore, FFT was applied, and the analysis time (T_0) was selected in consideration of the period component of the response and the load, with its duration being longer than that of the excited load. In the case of the Manjil earthquake, Δt was 0.005 s, and the number of data points (N) was 10784. The analysis time (T_0) was then calculated using Equation (20). Here, the size of the first load and the magnitude of the load after the end of the load measurement were assumed to be zero, and zero padding was performed.

$$T_0 = (10784 - 1) \times 0.05 \text{ sec} = 53.915 \text{ sec} \tag{20}$$

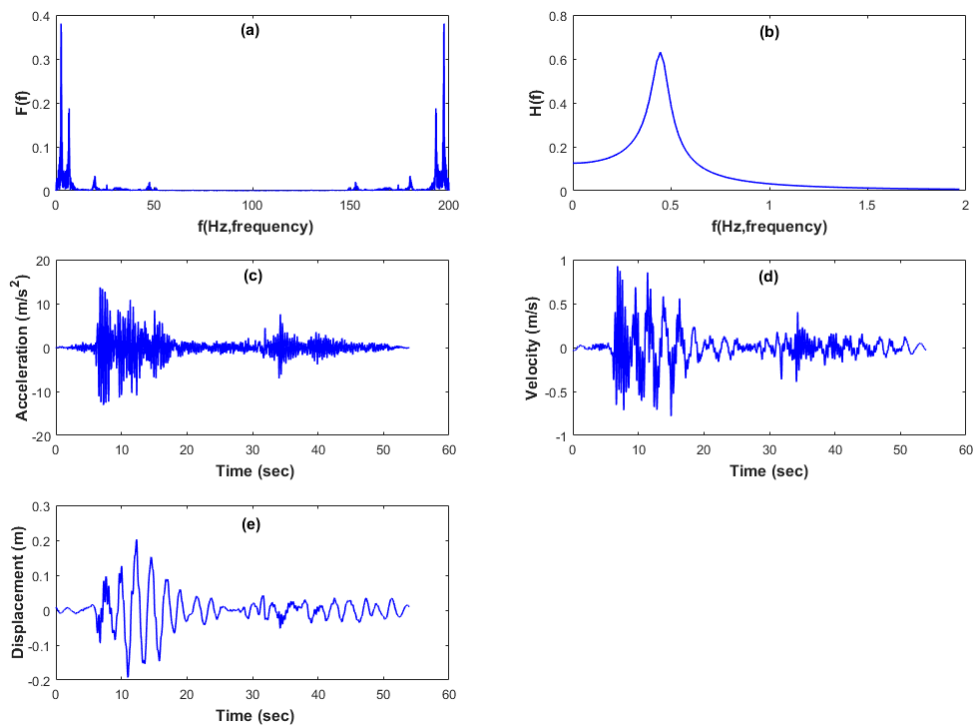


Figure 12. Analysis process for the 10th-story acceleration in the Manjil earthquake using Method 1: (a) discrete Fourier Transform of the applied load; (b) transfer function; (c) acceleration; (d) velocity; and (e) displacement.

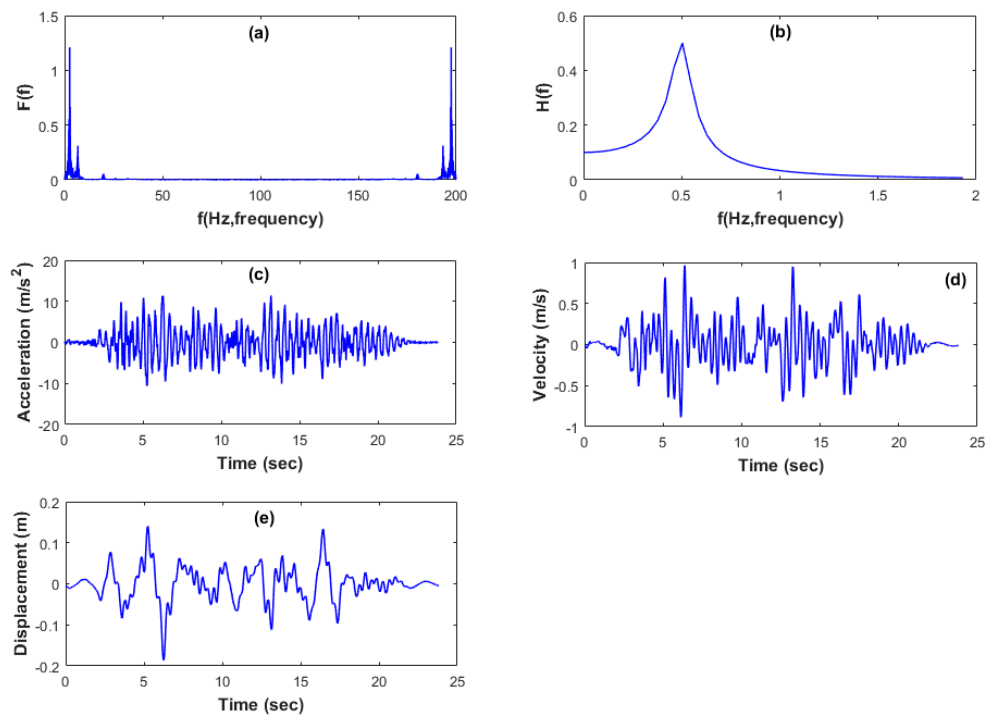


Figure 13. Analysis process for the 10th-story acceleration in the Superstition Hills earthquake using Method 1: (a) discrete Fourier Transform of the applied load; (b) transfer function; (c) acceleration; (d) velocity; and (e) displacement.

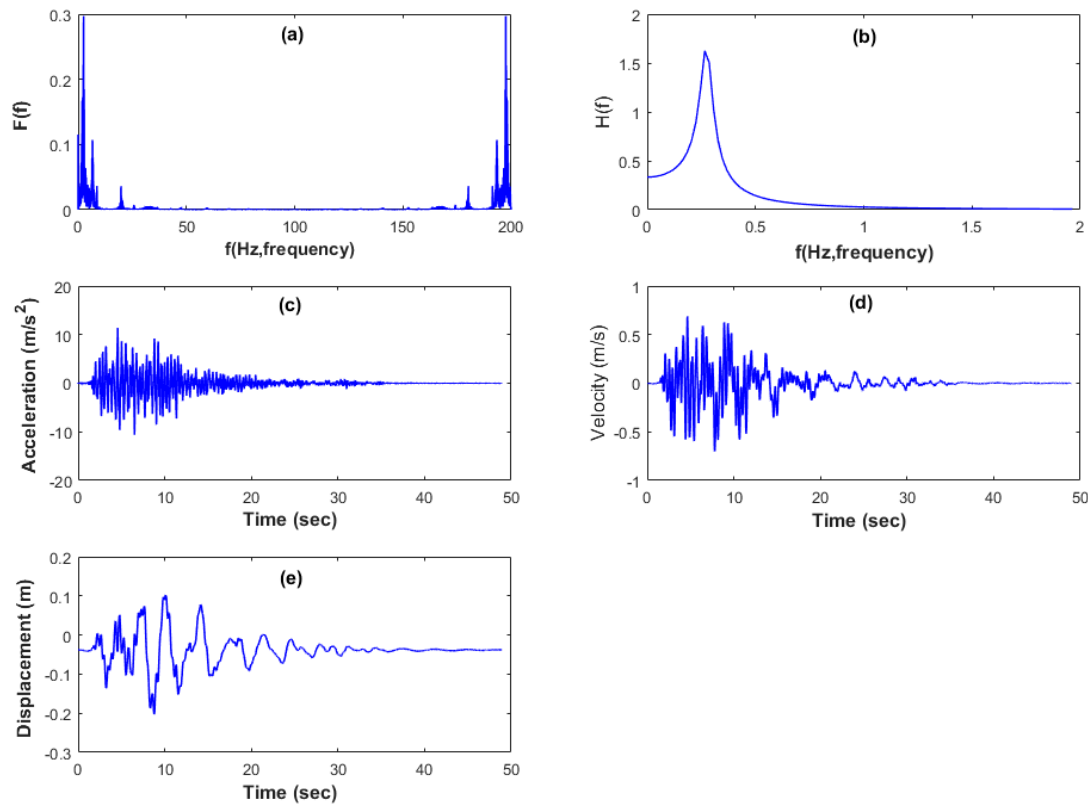


Figure 14. Analysis process for the 10th-story acceleration in the Kobe earthquake using Method 1: (a) discrete Fourier Transform of applied load; (b) transfer function; (c) acceleration; (d) velocity; and (e) displacement.

Next, the discrete Fourier transform of the applied load was performed. When the applied load in the time domain is converted into the frequency domain using the discrete Fourier transform (DFT), the discrete Fourier transform $F(f)$ is calculated. The $F(f)$ of the applied load of the Manjil earthquake is shown in Figure 12a, that of the Superstition Hills earthquake is shown in Figure 13a, and that of the Kobe earthquake is shown in Figure 14a. In the discrete Fourier transform $F(f)$ of the excited load of the Manjil earthquake, the sampling frequency (f_s), the maximum frequency (f_{max}), and the frequency interval (Δf) were obtained from Equations (21) to (23).

$$f_s = \frac{1}{\Delta t} = \frac{1}{0.005} = 200 \text{ Hz} \tag{21}$$

$$f_{max} = \frac{f_s}{2} = \frac{200}{2} = 100 \text{ Hz} \tag{22}$$

$$\Delta f = \frac{1}{T_0} = \frac{1}{53.915} = 0.018548 \text{ Hz} \tag{23}$$

Next, the complex frequency response function (or compliance) $H(f)$ was calculated using Equation (12). The complex frequency response function $H(f)$ of the Manjil earthquake is shown in Figure 12b, that of the Superstition Hills earthquake is shown in Figure 13b, and that of the Kobe earthquake is shown in Figure 14b. The responses of the displacement (U_d), velocity (U_v), and acceleration (U_a) in the frequency domain were obtained using Equations (24) to (26) by multiplying the complex frequency response function and the load by the frequency in the frequency domain.

$$U_d(\omega_j) = H(\omega_j)F(\omega_j) \tag{24}$$

$$U_v(\omega_j) = i\omega_j U_d(\omega_j) \tag{25}$$

$$U_a(\omega_j) = -\omega_j^2 U_d(\omega_j) \quad (26)$$

The displacement (U_d), velocity (U_v), and acceleration (U_a) responses in the frequency domain were obtained using the discrete Fourier inverse transform of the response (u), velocity (\dot{u}), and acceleration (\ddot{u}) in the time domain. The displacement (u) in the time domain was obtained using the discrete Fourier inverse transformation of Equation (27), the displacement (U_d) in the frequency domain was calculated using Equation (24). The displacement (u) in the time domain of the Manjil earthquake is shown in Figure 12e, that of the Superstition Hills earthquake in Figure 13e, and that of the Kobe earthquake in Figure 14e.

$$u(t) = F^{-1}\{U_d(f)\} \quad (27)$$

The velocity (\dot{u}) in the time domain is determined by the discrete Fourier inverse transformation, as in Equation (28), and the velocity (U_v) by the frequency domain estimated using Equation (25). The displacement (u) in the time domain of the Manjil earthquake is shown in Figure 12d, that of the Superstition Hills earthquake in Figure 13d, and that of the Kobe earthquake in Figure 14d.

$$\dot{u}(t) = F^{-1}\{U_v(f)\} \quad (28)$$

The acceleration (\ddot{u}) in the time domain was obtained using the discrete Fourier inverse transformation in Equation (29) with respect to acceleration (U_a), and in the frequency domain this was calculated as per Equation (26). The acceleration (\ddot{u}) in the time domain of the Manjil earthquake is shown in Figure 12c, that of the Superstition Hills earthquake in Figure 13c, and that of the Kobe earthquake in Figure 14c.

$$\ddot{u}(t) = F^{-1}\{U_a(f)\} \quad (29)$$

Here, as mentioned in the discrete Fourier transform of the load, before the discrete Fourier inverse transformation, the response in the frequency domain needs to be made a symmetrical complex conjugate with respect to f_{max} on the right and left sides [33].

The damping ratios of high-rise buildings are related to their shape, dimensions, room size, etc., and these were determined to be 3.5~21.7%, based on room size [38]. The average value, 10%, was selected for the Method 1; however, the results of Method 1 were not much affected by the damping ratios. In addition, the baseline drifts were not corrected in Method 1; therefore, the initial value of the displacement graphs did not start at zero point, meaning that zero padding is required.

3.3.2. Method 2

Figures 15–17 show the results of converting the accelerations of the Manjil, Superstition Hills, and Kobe earthquakes using Method 2. Method 2 computes the discrete data of the input seismic waves as the sum of the cosine functions using the cosine Fourier transform. The load magnitude after the first load and after the end of the measured load are assumed to be zero. There is zero padding. First, the acceleration (a_0) in the time domain is prepared and integrated so as to obtain the velocity (v_0) and the displacement (d_0). Baseline correction of the initial acceleration (a_0) was performed using the 1st-order equation. Then, the corrected acceleration (a) was integrated to calculate the new velocity (v) and the displacement (d). Finally, the displacement (d) was cosine corrected. Using the cosine Fourier series transform, the discrete input data were calculated as the sum of the cosine functions.

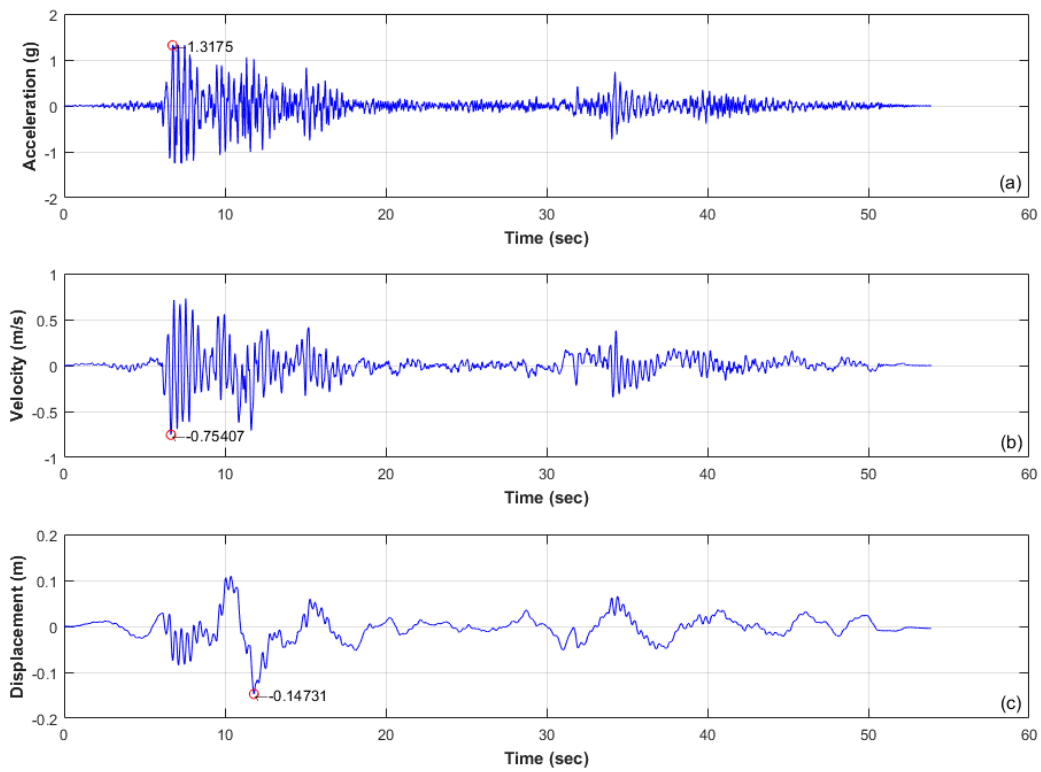


Figure 15. Analysis process for the 10th-story acceleration during the Manjil earthquake using Method 2; (a) acceleration; (b) velocity; (c) displacement.

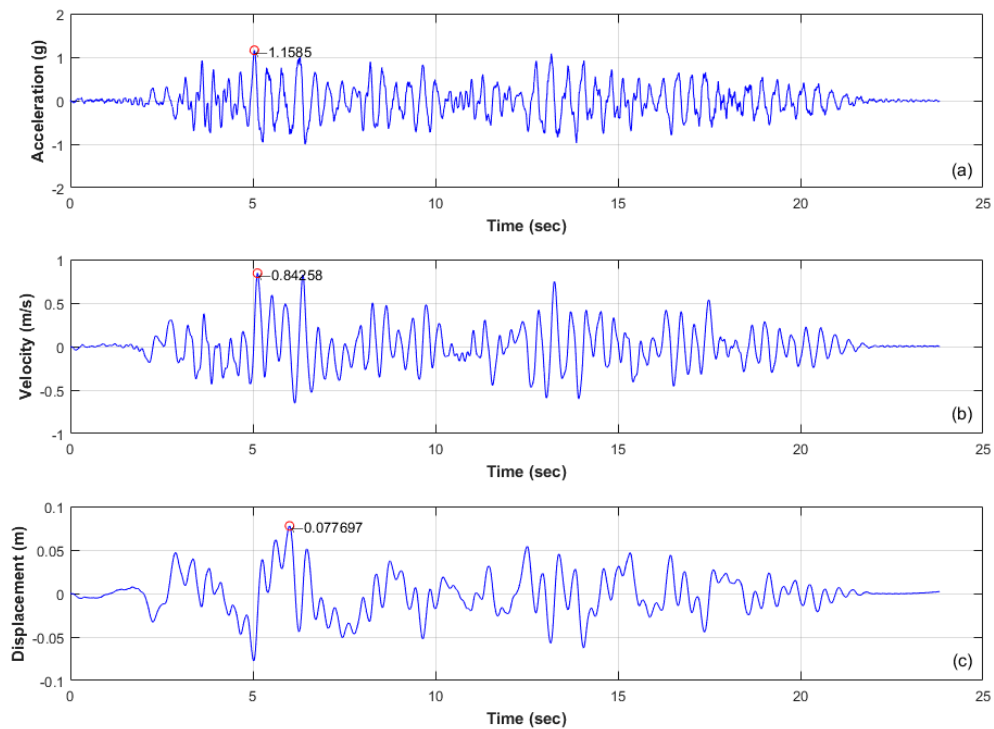


Figure 16. Analysis process for the 10th-story acceleration during the Superstition Hills earthquake using Method 2; (a) acceleration; (b) velocity; (c) displacement.

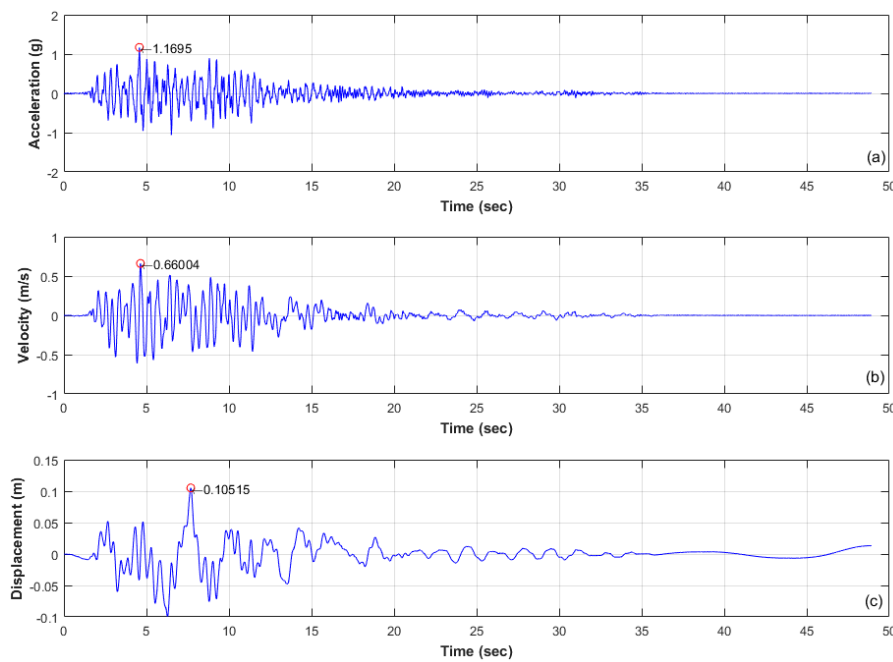


Figure 17. Analysis process for the 10th-story acceleration during the Kobe earthquake using Method 2; (a) acceleration; (b) velocity; (c) displacement.

3.3.3. Method 3

Figures 18–20 show the results of converting the accelerations of the Manjil, Superstition Hills, and Kobe earthquakes using Method 3. The Butterworth filter is a type of signal processing filter designed to have a frequency response that is as flat as possible in the passband [11]. It is also used to refer to a maximally flat magnitude filter. It was first described in 1930 by the British engineer and physicist, Stephen Butterworth, in his paper entitled “On the Theory of Filter Amplifiers”. The filter is a 4th-order Butterworth filter design and a high-pass filter that passes through the $0.1 f_c$ section. In addition, f_c is $\frac{1}{2}$ of the sample frequency, and is also referred to as the cutoff frequency or Nyquist frequency.

The magnitude of the frequency response $G(\omega)$ of an n -order Butterworth low-pass filter is given in terms of the transfer function $H(i\omega)$ as

$$G^2(\omega) = |H(i\omega)|^2 = \frac{G_0^2}{1 + \left(\frac{i\omega}{i\omega_c}\right)^{2n}} \tag{30}$$

where n is the order of the filter, which is 4 in this study; ω_c is the cutoff frequency, which in this study is 0.03; and G_0 is the frequency response at a frequency of zero.

3.4. Comparison of Acceleration Data Converted to Velocity and Displacement

Figure 21 compares the displacements at the roof of the tested model, estimated on the basis of high-speed imaging and analysis, with the displacements obtained based on conversion from acceleration data. Method 2 (baseline and cosine correction of the acceleration data) and Method 3 (least-square fitting and Butterworth filter) provided analyzed displacements that were closer to those measured than Method 1 (Penzien filter) did. Method 1 showed a substantial difference from the actual displacement. The differences between the analyzed and measured results occurred because Method 1 analyzed the raw data without zero padding, baseline correction or the least-squares method. The errors of displacement would have accumulated as a result of integrating the acceleration data twice, as shown in Figure 21. Also, $H_2(\omega)$ is a value that reflects the dynamic characteristics of the

structure, and can be calculated differently depending on the mass and stiffness of the structure. When it is difficult to accurately calculate the stiffness, the converted displacement differs from the actual value. The output of Method 3 depends on the degree of the Butterworth filter and the cutoff frequency. As shown by the National Disaster Management Institute (2012) [15], it is necessary to determine the cutoff frequency based on the number of samples per second.

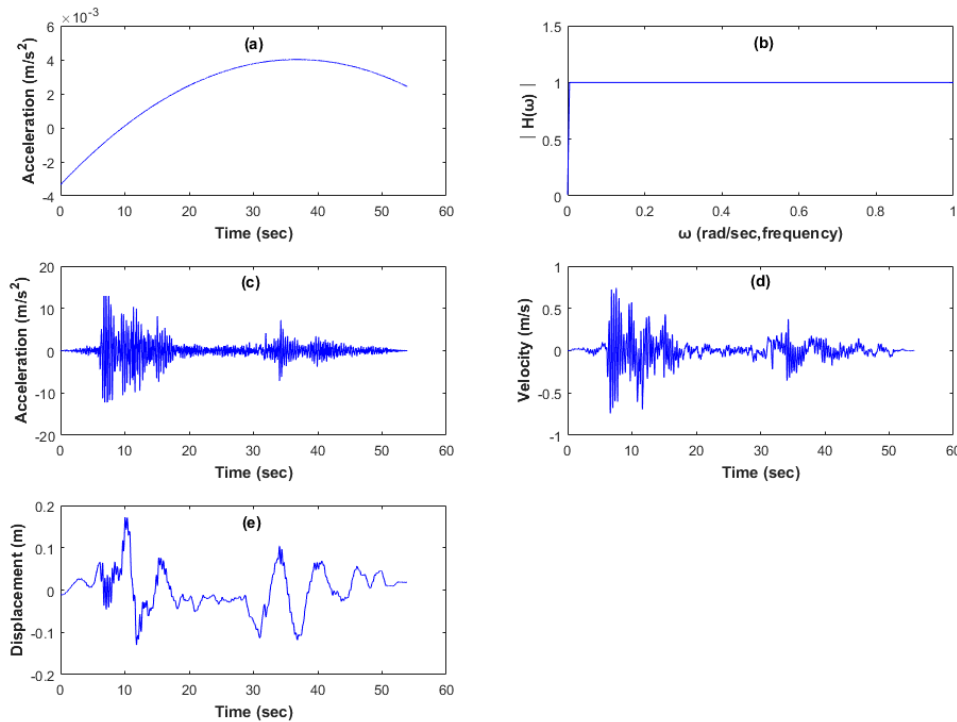


Figure 18. Analysis process for the 10th-story acceleration during the Manjil earthquake using Method 3: (a) 2nd-order polynomial equation for correcting acceleration; (b) 4th-order Butterworth high-pass filter; (c) acceleration; (d) velocity; (e) displacement.

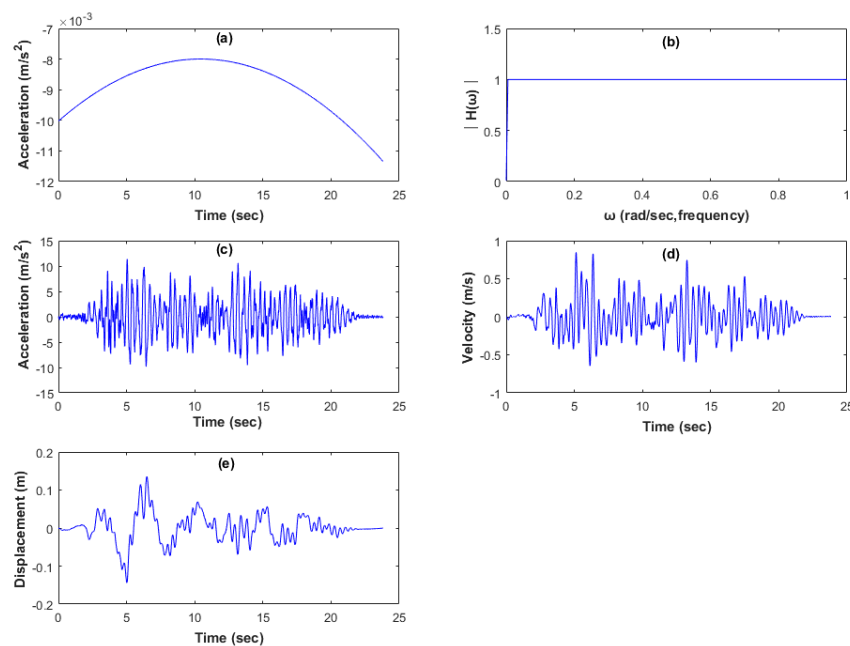


Figure 19. Analysis process for the 10th-story acceleration during the Superstition Hills earthquake using Method 3: (a) 2nd-order polynomial equation for correcting acceleration; (b) 4th-order Butterworth high-pass filter; (c) acceleration; (d) velocity; (e) displacement.

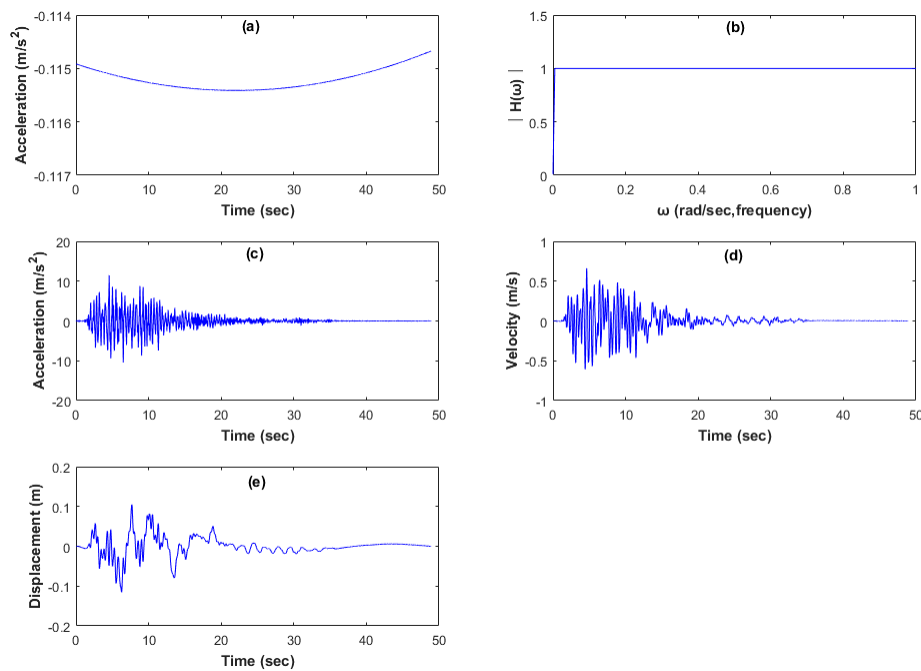


Figure 20. Analysis process for the 10th-story acceleration during the Kobe earthquake using Method 3: (a) 2nd-order polynomial equation for correcting acceleration; (b) 4th-order Butterworth high-pass filter; (c) acceleration; (d) velocity; (e) displacement.

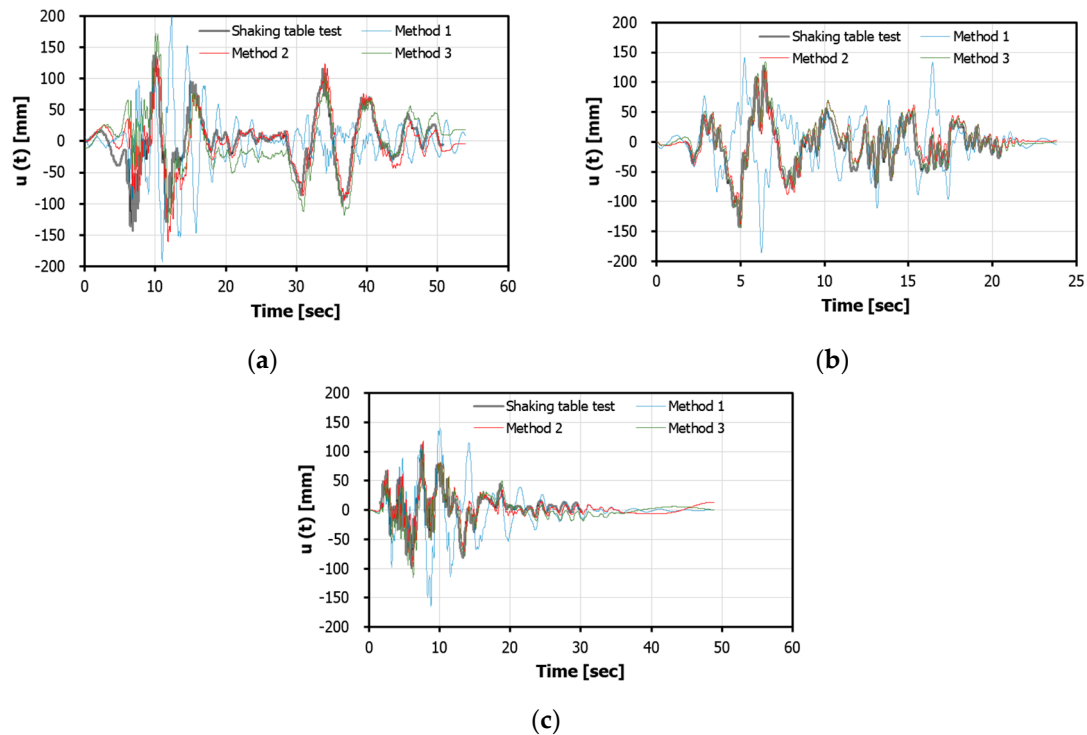


Figure 21. Comparison of measured displacement with displacements converted from acceleration data: (a) Manjil earthquake; (b) Superstition Hills earthquake; (c) Kobe earthquake.

4. Conclusions

In this study, the shake table test was performed to verify the conversion methods that were employed to convert acceleration data measured in a high-rise building into velocity and displacement data. Then, the displacement obtained by high-speed imaging during the shaking table test was

compared with the displacement obtained by processing acceleration data. This study applied three methods for the correction and conversion of acceleration data into velocity and displacement data. The resulting characteristics and applicability of the conversion methods for evaluating the diagnosis of high-rise buildings were derived as follows.

Method 1 used the transfer function $H_2(\omega)$, which reflects the dynamic characteristics of the system. Displacements converted using this method showed the lowest accuracy, because the transfer function depends on the dynamic characteristics of the structure. Method 1 did not use the zero padding and baseline correction methods. Therefore, even if discrete Fourier transformation was employed, there were a lot of differences between the analyzed and measured displacement values occurring based on a non-fixed starting point and the integration of acceleration.

Method 2 used the cosine Fourier series transform and baseline correction. Discrete input data was calculated as the sum of the cosine functions. Method 2 used the zero padding and baseline correction techniques in order to correct the initial value of the displacement. In this way, the accumulated displacement errors were corrected. Furthermore, even though the cosine correction filter functions in the time domain, the displacements were very close to the experimental values.

Method 3 used the least-squares fitting in the first step in order to remove the linear drift in the acceleration, and applied a high-pass Butterworth filter.

Method 3 did not use a zero padding; however, least-square fitting was used as the first filter. After that, the corrected acceleration data was passed through a Butterworth filter. The first filtered data was used to make the second filter efficient. Therefore, the analyzed data obtained using Method 3 are also very close to the experimental data.

For this study, there were a number of reasons for which a scale model was implemented: (1) The researchers had difficulty obtaining real data for a high-rise building; and (2) if the scale building model was to be used, the conditions and data related to strong-motion would be simplified. However, if the AVD methods for this study were applied to a real high-rise building, the accuracy would decrease.

Furthermore, the techniques adopted for these three methods could be separated and combined with each other. Based on Methods 1~3, the application and importance of each method is known. Based on this research, the analytical method for converting acceleration into displacement can be summarized by the following three steps:

1. First step: A technique is required to establish a fixed point, so that the integration of acceleration data will not be subject to accumulated errors.
2. Second step: Methods for eliminating baseline drift are also taken into consideration, including baseline correction filters and least-square fitting. These could be referred to as a first filter.
3. Third step: After these 2 steps, the noise contained in the real data needs to be eliminated. This step is the most important step. There are many potential second filters, including discrete Fourier transformation (Method 1), the cosine correction filter (Method 2), and the Butterworth filter (Method 3).

The displacements converted by Method 2 proved to be the most reliable when compared with displacements measured in the shaking table test. In addition, it is necessary to further investigate the limitations and applicability of the conversion methods for the purpose of estimating the reliable displacement of high-rise buildings.

Author Contributions: H.H., Y.B., and J.K. conceived and designed the analysis and the experiments; S.P. and J.K. performed the experiment; M.P. analyzed the data; H.H. and M.P. wrote the paper.

Funding: This study was supported by the National Research Council of Science & Technology (NST) grant by the Korea government (No. CRC-16-02-KICT).

Acknowledgments: The authors would like to thank the four anonymous reviewers, whose constructive comments improved the paper.

Conflicts of Interest: The authors declare no conflict of interest.

References

1. Darragh, B.; Silva, W.; Gregor, N. Strong motion record processing for the PEER center. In Proceedings of the COSMOS Invited Workshop on Strong-Motion Record Processing, Richmond, CA, USA, 26–27 May 2004; pp. 26–27.
2. Mollova, G. Effects of digital filtering in data processing of seismic acceleration records. *Eurasip J. Adv. Signal Process.* **2007**, *2007*, 029502. [[CrossRef](#)]
3. Ambraseys, N.; Smit, P.; Douglas, J.; Margaritis, B.; Sigbjörnsson, R.; Olafsson, S.; Suhadolc, P.; Costa, G. Internet site for European strong-motion data. *Boll. Geofis. Teor. Appl.* **2004**, *45*, 113–129.
4. Jones, J.; Kalkan, E.; Stephens, C.; Ng, P. Prism, processing and review interface for strong motion data software. In *Eleventh U.S. National Conference on Earthquake Engineering; Integrating Science, Engineering & Policy*: Los Angeles, CA, USA, 2018.
5. Jones, J.; Kalkan, E.; Stephens, C. *Processing and Review Interface for Strong Motion Data (Prism) Software, Version 1.0. 0—Methodology and Automated Processing*; 2331-1258; US Geological Survey: Reston, VA, USA, 2017.
6. Jones, J.; Kalkan, E.; Stephens, C.; Ng, P.J.S.R.L. PRISM Software: Processing and Review Interface for Strong-Motion Data. *Seismol. Res. Lett.* **2017**, *88*, 851–866. [[CrossRef](#)]
7. Luzi, L.; Puglia, R.; Russo, E.; D’Amico, M.; Felicetta, C.; Pacor, F.; Lanzano, G.; Çeken, U.; Clinton, J.; Costa, G.J.S.R.L. The engineering strong-motion database: A platform to access pan-European accelerometric data. *Seismol. Res. Lett.* **2016**, *87*, 987–997. [[CrossRef](#)]
8. Luzi, L.; Puglia, R.; Russo, E.; D’Amico, M.; Lanzano, G.; Pacor, F.; Felicetta, C. Engineering Strong-Motion database: a gateway to access European strong motion data. In Proceedings of the 16th World Conference on Earthquake Engineering, Santiago, Chile, 9–13 January 2017.
9. Scordilis, E.; Theodoulidis, N.; Kalogeras, I.; Margaritis, B.; Klimis, N.; Stewart, J.; Boore, D.; Seyhan, E.; Savvaidis, A.; Mylonakis, G. Strong Motion Database for Crustal Earthquakes in Greece and Surrounding Area. In Proceedings of the 16th European conference on “Earthquake Engineering”, Thessaloniki, Greece, 18–21 June 2018.
10. Puglia, R.; Russo, E.; Luzi, L.; D’Amico, M.; Felicetta, C.; Pacor, F.; Lanzano, G. Strong-motion processing service: A tool to access and analyse earthquakes strong-motion waveforms. *Bull. Earthq. Eng.* **2018**, *16*, 2641–2651. [[CrossRef](#)]
11. Butterworth, C.J.E. Filter approximation theory. *Engineer* **1930**, *7*, 536–541.
12. Van Valkenburg, M.E. *Analog Filter Design*; Holt, Rinehart, and Winston: New York, NY, USA, 1982.
13. Tsuchihashi, T.; Yasuda, M. Rapid Diagnosis Systems Using Accelerometers in Seismic Damage of Tall Buildings. *Int. J. High Rise Build.* **2017**, *6*, 207–216. [[CrossRef](#)]
14. Chiu, H.-C. Stable baseline correction of digital strong-motion data. *Bull. Seismol. Soc. Am.* **1997**, *87*, 932–944.
15. Chiu, H.-C. A Compatible Baseline Correction Algorithm for Strong-Motion Data. *Terr. Atmos. Ocean. Sci.* **2012**, *23*, 171–180. [[CrossRef](#)]
16. Malhotra, P.K. Response spectrum of incompatible acceleration, velocity and displacement histories. *Earthq. Eng. Struct. Dyn.* **2001**, *30*, 279–286. [[CrossRef](#)]
17. Pecknold, D.; Riddell, R. Effect of initial base motion on response spectra-closure. *J. Eng. Mech. Div. Asce* **1979**, *105*, 1057–1060.
18. Pecknold, D.A.; Riddell, R. Effect of initial base motion on response spectra. *J. Eng. Mech. Div.* **1978**, *104*, 485–491.
19. Athanasiou, A.; Oliveto, G.; Ponzio, F.J.E.S. Baseline correction of digital accelerograms from field testing of a seismically isolated building. *Earthq. Spectra* **2018**, *34*, 915–939. [[CrossRef](#)]
20. Cherry, S. Earthquake ground motions: Measurement and characteristics. In *Engineering Seismology and Earthquake Engineering*; Soines, N., Ed.; Springer: Berlin/Heidelberg, Germany, 1974; p. 315.
21. Agnew, D.C.; Berger, J. Vertical seismic noise at very low frequencies. *J. Geophys. Res. Solid Earth* **1978**, *83*, 5420–5424. [[CrossRef](#)]
22. Crombie, D.D.; Hasselmann, K.; Sell, W. High-frequency radar observations of sea waves travelling in opposition to the wind. *Bound. Layer Meteorol.* **1978**, *13*, 45–54. [[CrossRef](#)]
23. Kanai, K.; Tanaka, T. On microtremor VIII. *Bull. Earthq. Res. Inst. Univ. Tokyo* **1961**, *39*, 97–114.

24. Metz, A.; Wolf, M.; Achermann, P.; Scholkmann, F. A new approach for automatic removal of movement artifacts in near-infrared spectroscopy time series by means of acceleration data. *Algorithms* **2015**, *8*, 1052–1075. [[CrossRef](#)]
25. Boore, D.M.; Bommer, J.J. Processing of strong-motion accelerograms: Needs, options and consequences. *Soil Dyn. Earthq Eng.* **2005**, *25*, 93–115. [[CrossRef](#)]
26. Park, S.; Park, H.; Kim, J.; Adeli, H.J.M. 3D displacement measurement model for health monitoring of structures using a motion capture system. *Measurement* **2015**, *59*, 352–362. [[CrossRef](#)]
27. Kasai, K.; Ito, H.; Ooki, Y.; Hikino, T.; Kajiwara, K.; Motoyui, S.; Ozaki, H.; Ishii, M. Full scale shake table tests of 5-story steel building with various dampers. In Proceedings of the 7th International Conference on Urban Earthquake Engineering (7CUUE) & 5th International Conference on Earthquake Engineering (5ICEE), Tokyo, Japan, 3–5 March 2010; pp. 11–22.
28. Lu, X.; Chen, Y.; Mao, Y. Shaking table model test and numerical analysis of a supertall building with high-level transfer storey. *Struct. Des. Tall Spec. Build.* **2012**, *21*, 699–723. [[CrossRef](#)]
29. Lu, X.; Zou, Y.; Lu, W.; Zhao, B. Shaking table model test on shanghai world financial center tower. *Earthq. Eng. Struct. Dyn.* **2007**, *36*, 439–457. [[CrossRef](#)]
30. Lu, X.; Lu, X.; Guan, H.; Ye, L. Collapse simulation of reinforced concrete high-rise building induced by extreme earthquakes. *Earthq. Eng. Struct. Dyn.* **2013**, *42*, 705–723. [[CrossRef](#)]
31. Park, J.-W.; Sim, S.-H.; Jung, H.-J. Development of a wireless displacement measurement system using acceleration responses. *Sensors* **2013**, *13*, 8377–8392. [[CrossRef](#)] [[PubMed](#)]
32. Clough, R.; Penzien, J. *Dynamics of Structures*, 3rd ed.; Computers & Structures, Inc.: Berkeley, CA, USA, 2003.
33. Kim, D. *Dynamics of Structures 4th*; Goomi Book: Seoul, Korea, 2017.
34. Park, B.C.; Jin, Y.J.; Lim, K.H.; Seong, J.Y.; Park, K.J. *Development of the Public Buildings Emergency Integrity Assessment Technology Using Seismic Acceleration Response Signal*; National Disaster Management Institute: Seoul, Korea, 2012; pp. 1–292.
35. Guorui, H.; Tao, L. Review on Baseline Correction of Strong-Motion Accelerogram. *Int. J. Sci. Technol. Soc.* **2015**, *3*, 309–314. [[CrossRef](#)]
36. Boore, D.M.; Stephens, C.D.; Joyner, W.B. Comments on Baseline Correction of Digital Strong-Motion Data: Examples from the 1999 Hector Mine, California, Earthquake. *Bull. Seismol. Soc. Am.* **2002**, *92*, 1543–1560. [[CrossRef](#)]
37. FEMA. *Quantification of Building Seismic Performance Factors, FEMA P-695*; Applied Technology Council for the Federal Emergency Management Agency: Washington, DC, USA, 2009.
38. Ahn, S.-K.; Jeong, H.-I.; La, W. Estimation of Damping Ratio for Floor slabs of Building Structure. In *Proceedings of the Korean Society for Noise and Vibration Engineering Conference, 2009*; The Korean Society for Noise and Vibration Engineering: Seoul, Korea, 2009.



© 2019 by the authors. Licensee MDPI, Basel, Switzerland. This article is an open access article distributed under the terms and conditions of the Creative Commons Attribution (CC BY) license (<http://creativecommons.org/licenses/by/4.0/>).